J. Fluid Mech. (1998), *vol.* 364, *pp.* 59–80. Printed in the United Kingdom

Spatio-temporal character of non-wavy and wavy Taylor–Couette flow

By STEVEN T. WERELEY AND RICHARD M. LUEPTOW
Department of Mechanical Engineering, Northwestern University, Evanston, IL 60208, USA

(Received 14 February 1997 and in revised form 12 September 1997)

The stability of supercritical Couette flow has been studied extensively, but few measurements of the velocity field of flow have been made. Particle image velocimetry (PIV) was used to measure the axial and radial velocities in a meridional plane for non-wavy and wavy Taylor–Couette flow in the annulus between a rotating inner cylinder and a fixed outer cylinder with fixed end conditions. The experimental results for the Taylor vortex flow indicate that as the inner cylinder Reynolds number increases, the vortices become stronger and the outflow between pairs of vortices becomes increasingly jet-like. Wavy vortex flow is characterized by azimuthally wavy deformation of the vortices both axially and radially. The axial motion of the vortex centres decreases monotonically with increasing Reynolds number, but the radial motion of the vortex centres has a maximum at a moderate Reynolds number above that required for transition. Significant transfer of fluid between neighbouring vortices occurs in a cyclic fashion at certain points along an azimuthal wave, so that while one vortex grows in size, the two adjacent vortices become smaller, and vice versa. At other points in the azimuthal wave, there is an azimuthally local net axial flow in which fluid winds around the vortices with a sense corresponding to the axial deformation of the wavy vortex tube. These measurements also confirm that the shift-and-reflect symmetry used in computational studies of wavy vortex flow is a valid approach.

1. Introduction

Supercritical circular Couette flow between concentric cylinders, the inner cylinder rotating and the outer cylinder fixed, has been studied in great depth since Taylor's pioneering experiments and analysis (Taylor 1923). Most research has been directed toward the stability of the flow with little attention to the velocity field that develops in the annulus. Nevertheless, an understanding of the velocity field is crucial to engineering applications of the flow such as rotating filter separators used for the separation of blood and oily emulsions.

Several limited measurements of the velocity in Taylor vortex flow have been made. Heinrichs *et al.* (1988) used laser Doppler velocimetry (LDV) to measure the axial velocity (v_z) in Taylor vortex flow at a series of points distributed in the axial direction for a fixed radial position. Gollub & Freilich (1976) and Berland, Jøssang & Feder (1986) made similar measurements of the radial velocity (v_r) at a fixed radial position and several axial positions using LDV. Wereley & Lueptow (1994) generated contour plots of the azimuthal velocity (v_θ) based on extensive LDV measurements over a two-dimensional (r, z) grid of about 300 points per vortex pair. All of these experiments were used to confirm the validity of Davey's (1962) perturbation expansion of the Navier–Stokes equations about the circular Couette flow solution, particularly that the

vortices strengthen with increasing rotating Reynolds number, $Re = r_i \Omega d/\nu$, where Ω is the angular velocity of the inner cylinder, $d = r_o - r_i$ is the gap between the outer cylinder of radius r_o and the inner cylinder of radius r_i, and ν is the kinematic viscosity.

Higher-order supercritical circular Couette flow regimes, as categorized by Andereck, Liu & Swinney (1986), include wavy vortex flow, modulated wavy vortex flow, and turbulent Taylor vortex flow. Only a few experimental measurements of the velocity field for these flow regimes have been made. Gollub & Swinney (1975) and Brandstater & Swinney (1987) measured the time dependence of the radial velocity (v_r) at a single location in the annulus for a large range of Reynolds numbers using LDV to demonstrate that the Landau picture of the transition to turbulence is not accurate and to determine that the attractor dimension is 2 for wavy vortex flow. Wereley and Lueptow (1994) measured the two-dimensional (r, z) spatial distribution of the time-averaged azimuthal velocity (v_θ) for wavy, modulated wavy, and turbulent vortex flow based on LDV measurements. They found that the magnitude of the radial gradient of azimuthal velocity increases near both the inner and outer cylinders and that the radial outflow region between adjacent vortices becomes more jet-like as the Reynolds number increases. Unfortunately, only time-averaged velocity contours could be obtained because LDV was used. A few limited space–time measurements of wavy vortex flow have been made recently. Takeda, Fischer & Sakakibara (1994) used an ultrasonic Doppler velocity profile method to measure the one-dimensional space–time (z, t) dependence of the axial velocity (v_z) in wavy vortex flow. Their results indicate that the axial velocity dependence on axial position and time for wavy vortex flow can be decomposed into three fundamental wavenumber-frequency modes. Ultrafast NMR imaging was used by Kose (1994) to measure the two-dimensional space (r, z) dependence of the radial velocity (v_r) for wavy vortex flow, but the sampling rate was too slow to adequately resolve the time dependence of the flow.

Numerical simulations of Taylor vortex flow and wavy vortex flow have been successful in providing some information about the velocity field (Meyer 1967; Meyer 1969; Majumdar & Spalding 1977; Meyer-Spasche & Keller 1980; Jones 1981; Moser, Moin & Leonard 1983; Fasel & Booz 1984; Marcus 1984; Jones 1985; Schroder & Keller 1990). Nevertheless, most of these studies focused on the computational methods, were aimed at specific cases, or provided minimal information about the velocity field. Marcus' detailed results and analysis are a notable exception (Marcus 1984). From his computational results, he conjectured that the travelling waves are a secondary instability related to the strong radial motion at outflow boundaries between vortices. His results also indicate that the waviness results in fluid being mixed between adjacent vortices.

The few measurements of the velocity field for Taylor–Couette flow made by previous researchers have been limited in scope. In most cases, only a single velocity component was measured as a function of axial position for Taylor vortex flow, which is steady, or as a function of time at a single location for unsteady wavy vortex flow. In a few cases a single velocity component was measured as a function of axial position while resolving the time dependence or in the (r, z)-plane without resolving the time dependence. By contrast, we present here measurements of two velocity components in a plane while resolving the time dependence. Specifically, we present here the first time-resolved two-dimensional (r, z, t) measurements of both the radial and axial velocities (v_r, v_z) as a function of Reynolds number for both non-wavy Taylor vortex flow and wavy vortex flow with the inner cylinder rotating and the outer cylinder fixed.

The particle image velocimetry (PIV) measurements of the velocity field for supercritical circular Couette flow described in this paper were aimed toward several

objectives. The first objective was to measure accurately the velocity field in non-wavy Taylor vortex flow and its dependence upon Reynolds number. The second objective was to measure the space- and time-dependent velocity field for wavy vortex flow. The third objective was to determine the degree to which fluid is transferred from one vortex to an adjacent vortex in wavy vortex flow and its dependence on time and Reynolds number. The fourth objective was to examine the dependence of the motion of vortices on Reynolds number for wavy vortex flow. The fifth and final objective was to experimentally determine the validity of the shift-and-reflect symmetry used in computational models of wavy vortex flow.

2. Experimental methods

The flow cell used for the experiments consisted of a pair of concentric cylinders, the inner acrylic one rotating and the outer glass one fixed. The inner cylinder had a radius of $r_i = 4.34$ cm and the outer cylinder had a radius of $r_o = 5.23$ cm resulting in a gap width of $d = 0.89$ cm and a radius ratio of $\eta = r_i/r_o = 0.830 \pm 0.003$. The two cylinders were held concentric by aluminium endcaps which also provided the fixed-end boundary conditions at the two axial extremes of the annulus. The aspect ratio, the ratio of the length of the annulus to the gap width, was $\Gamma = 47.7$. The outer cylinder was enclosed within a glass box and the space between the box and the outer cylinder was filled with index-of-refraction-matched fluid similar to the working fluid described below to prevent refraction at the curved surface of the outer cylinder.

The inner cylinder was driven by a stepper motor capable of microstepping at 25000 steps per revolution, producing a very smooth rotation. The rotational frequency of the inner cylinder was read by an optical encoder with a resolution of 300 pulses per revolution. These devices allowed computer control of the rotational speed of the inner cylinder to better than 0.1 % for the range of speeds used in these experiments.

The working fluid was a mixture of water, glycerol, sodium iodide, and trace amounts of sodium thiosulfate (to prevent a yellowish tint in the solution). The sodium iodide (57 wt %) was used to increase the index of refraction of the fluid to match that of glass so that the laser sheet and particle images were not refracted at the curved fluid–glass interface. Silver-coated hollow glass spheres (Potters Industries, NJ) with an average diameter of 14 μm were added as PIV seed particles in a volume concentration of about 1.0×10^{-4}. The particles had a density of 1.6 g cm^{-3}, which was slightly less than the density of the working solution, 1.7 g cm^{-3}. The densities of the particles and fluid were close enough so that the distribution of particles in suspension remained uniform for several hours. The nominal kinematic viscosity of the solution was 3.1 cSt at 20 °C.

Ensuring adequate control of the viscosity of the working fluid was difficult because the viscosity of aqueous solutions of glycerol are very sensitive to temperature changes. Because using a water jacket to control the temperature of the working fluid was impractical, the temperature of the working fluid was continuously monitored. The temperature of the working fluid tracked the room temperature, which varied by no more than ± 0.25 °C over the course of an experiment. The viscosity of the working fluid, which was measured before and after an experiment using a Canon–Fenske viscometer with an uncertainty of ± 0.2 %, never changed by more than 1 %.

The uncertainty in the Reynolds number, owing to the variation in the inner cylinder speed, fluid viscosity, and other factors, was at most 4 %. Estimating the uncertainty in the measured velocity data is difficult. The systematic uncertainty in the velocity measurements resides primarily in two areas: the ability of seed particles to follow the

flow and the accurate measurement of the particles' average displacement between images. The seed particles were assumed to follow the flow quite accurately because the Stokes number for the working fluid flowing over a single particle was several orders of magnitude less than 0.14, the maximum Stokes number for which a particle will accurately follow the flow (Dring 1982). Thus, the systematic uncertainty in the velocity measurement was related only to spatial resolution and laser pulse timing. Since a cross-correlation PIV algorithm was used to determine particles' average displacement between images, subpixel resolution was obtained (Willert & Gharib 1991). A worst case estimate of the particle displacement measurement error is $\pm 0.1\%$. The temporal resolution in the delay between laser pulses of a few nanoseconds over a period of 10 ms results in negligible error.

For each Reynolds number at which velocity measurements were made, the annulus was filled with fluid, and the inner cylinder was run at high speed for a few minutes to mix the fluid and particles thoroughly. Then the inner cylinder was stopped and the working fluid allowed to settle to quiescence. Finally, the inner cylinder speed was ramped linearly to the desired speed. Because of the sensitivity of the Taylor–Couette system to initial conditions, the acceleration up to each Reynolds number was held constant at a relatively slow value of $0.3\ Re\ s^{-1}$. After the inner cylinder reached the desired speed, the flow was allowed to develop at that Reynolds number for at least 10 min to ensure that the flow was fully developed before measurements began. Holding the inner cylinder speed constant and repeating the measurements some time later showed that this procedure generated repeatable results.

The flow velocities were measured using a TSI Particle Image Velocimetry system based on cross-correlating a pair of images to avoid directional ambiguity. An electronically shuttered 10 W argon laser was used to illuminate a radial-axial plane through the axis of the circular Couette flow device. The laser sheet had a thickness of 0.2 mm with $\pm 0.5\%$ variation in thickness in the measurement field. Since the through-sheet velocity in the azimuthal direction was so much larger than the measured axial and radial velocities, care was taken to assure that the laser sheet timing was short enough and the laser intensity great enough to capture a largely overlapping population of particles in two consecutive images, even near the inner cylinder where the through-sheet velocity is greatest. In some situations, a large through-sheet velocity at an off-axis angle to the PIV camera could be misinterpreted as an axial velocity component. In this case, perspective error was negligible because the imaged plane was smaller than the CCD camera lens resulting in paraxial light rays. It was also necessary to align the laser sheet precisely in a radial-axial plane to avoid anomalous apparent radial velocity components caused by the azimuthal path of the particles through the thickness of the laser sheet. In addition to careful visual alignment of the laser sheet with the axis of rotation, PIV measurements of stable circular Couette flow were used to ensure that the laser sheet was properly aligned. If the sheet were not in a radial axial-plane, radial velocity components would appear for circular Couette flow, whereas proper alignment resulted in zero radial velocity for stable circular Couette flow. Images of 640×200 pixels were captured at the axial centre of the flow cell, with the pixel dimension corresponding to 0.0045 cm. Velocity vectors were calculated at a grid of 31 points in the axial direction and nine points in the radial direction using an interrogation region of 32×32 pixels. Typically 175 image pairs were acquired at either 5 or 15 Hz, depending on the Reynolds number of the flow, using a TSI Cross-Correlation CCD camera. The time between laser pulses in each pair ranged from 0.0015 to 0.0125 s, depending on the Reynolds number. For certain measurements of the frequency content of the flow field, the spatial resolution was reduced to 200 by 32

pixels and over 8000 image pairs were collected, resulting in very accurate frequency measurements.

The critical rotating Reynolds number at the onset of Taylor vortex flow for $\eta = 0.83$ is $Re_c = 102$, based on a cubic spline fit to the data provided by DiPrima & Swinney (1985). Non-wavy Taylor vortex flow in the test cell was characterized by 24 pairs of vortices in the annulus. Wavy vortices were first easily detectable using PIV at $Re = 131$, or at a reduced Reynolds number of $\epsilon = Re/Re_c - 1 = 0.28$. Two waves around the annulus were detected for the 24 pairs of vortices. At $Re = 202$, $\epsilon = 0.98$, three waves appeared and the number of vortex pairs was reduced to 22. For $Re > 250$, $\epsilon > 1.45$, four waves appeared around the annulus, and the number of vortex pairs remained at 22.

3. Results and discussion

3.1. *Taylor vortex flow*

The velocity field in the radial-axial plane of the flow is shown in figure 1 for non-wavy Taylor vortex flow based on the ensemble average of six individual velocity vector fields. In this and subsequent figures, the annular gap is horizontal with the wall of the inner cylinder (IC) the upper horizontal line, and the wall of the outer cylinder (OC) the lower horizontal line. Vectors indicate velocity in the axial-radial plane. Contours represent the azimuthal velocity, which was calculated from the radial velocity and axial velocity using the axisymmetric azimuthal momentum equation. The azimuthal velocity, normalized with the surface speed of the inner cylinder, varies from unity at the inner cylinder to zero at the outer cylinder. Asterisks mark the vortex centres which were found based on the interpolated position of minimum speed in the radial plane, $(v_r^2 + v_z^2)^{1/2}$, using a weighted average over three consecutive time instants and nine spatially adjacent points. Figure 1(*a*) shows the velocity field at a Reynolds number of $Re = 103$, just above the transition to supercritical flow. Figure 1(*b*) shows the velocity field at $Re = 124$, slightly below the transition to wave vortex flow.

From the velocity vectors it is evident that the vortices grow substantially stronger as the Reynolds number increases as predicted analytically (Davey 1962) and computationally (Fasel & Booz 1984) and confirmed experimentally for single velocity components by other means (Snyder & Lambert 1966; Gollub & Freilich 1976; Berland *et al.* 1986; Heinrichs, *et al.* 1988; Tsameret & Steinberg 1994; Wereley & Lueptow 1994). The radial flow between vortices results in a deformation of the azimuthal velocity contours as high-speed fluid from near the inner cylinder is carried outward and low-speed fluid from near the outer cylinder is carried inward. Because of the stronger vortices, the deformation is greater at the higher Reynolds number in figure 1(*b*). It is also apparent that the radial outflow between vortices is substantially stronger than the radial inflow, most visible at the higher Reynolds number in Figure 1(*b*). The stronger outflow results in more sharply deformed azimuthal velocity contours at the outflow region than at the inflow region, consistent with direct measurements of the azimuthal velocity using laser Doppler velocimetry (Wereley & Lueptow 1994).

The radial velocity profile along an axial line at the centre of the annular gap and the axial velocity profile along a radial line through a vortex centre are shown in figure 2 for $Re = 103$ and $Re = 124$. The velocities are normalized by the surface speed of the inner cylinder. The axial position variable z is normalized by the annular gap d so that $\zeta = z/d$. The position variable in the radial direction, $\xi = (r - r_i)/d$, is normalized by the gap width so that it varies from $\xi = 0$ at the inner cylinder to $\xi = 1$ at the outer cylinder. The symbols are measured velocities corresponding to those in the vector

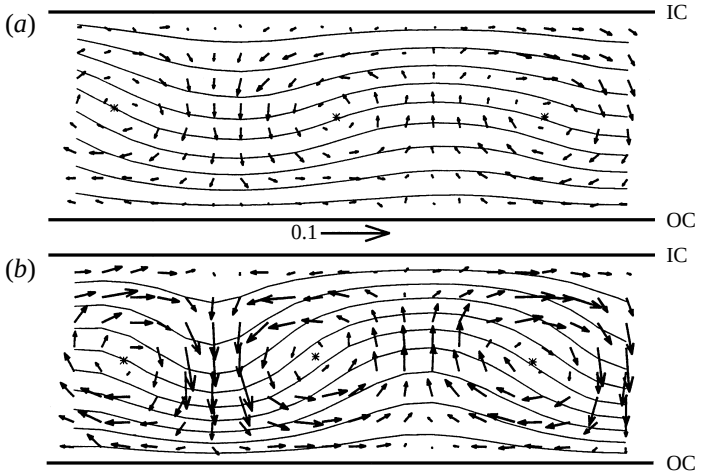

FIGURE 1. Radial-axial velocity vectors and contours of azimuthal velocity in a radial-axial plane for Taylor vortex flow. The rotating inner cylinder (IC) is the upper boundary and the fixed outer cylinder (OC) is the lower boundary of each frame. The velocity vectors are scaled identically in both figures with the arrow between the frames corresponding to $0.1\ r_i\Omega$. Contours are spaced at $0.1\ r_i\Omega$. (*a*) Just above transition to Taylor vortex flow, $Re = 103$, $\epsilon = 0.01$. (*b*) $Re = 124$, $\epsilon = 0.22$.

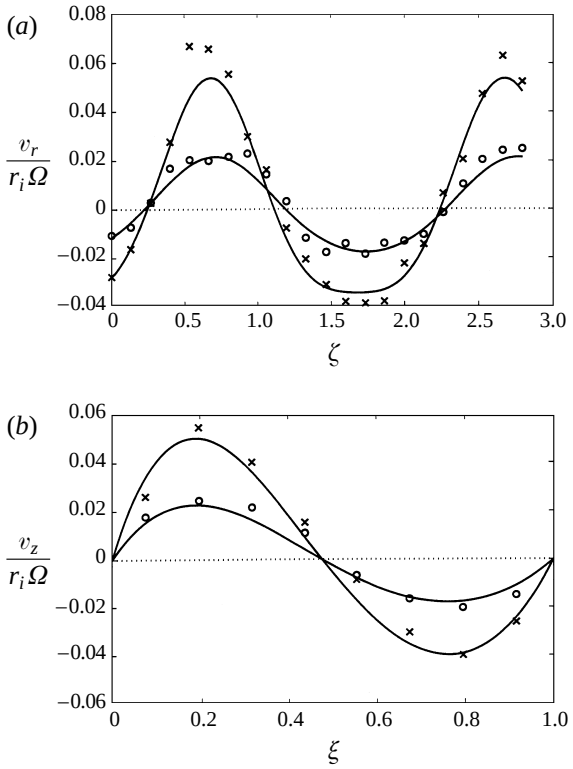

FIGURE 2. (*a*) Radial velocity normalized by the surface velocity of the inner cylinder along an axial line through the centre of the annular gap. (*b*) Axial velocity normalized by the surface velocity of the inner cylinder along a radial line through a vortex centre. ○, $Re = 103$, $\epsilon = 0.01$; ×, $Re = 124$, $\epsilon = 0.22$. Curves represent equation (1).

plots of figure 1. The curves represent the velocity profile based on the Davey perturbation expansion for Taylor–Couette flow (Davey 1962). The Davey expansion expresses the radial and axial velocities, v_r and v_z, as infinite series of the following form

$$v_r(r, z, \epsilon') = \sum_{n=1}^{\infty} A^n(\epsilon')\, u_n(r) \cos n\lambda(z - z_0), \tag{1a}$$

$$v_z(r, z, \epsilon') = \sum_{n=1}^{\infty} A^n(\epsilon') \frac{1}{n\lambda} w_n(r) \sin n\lambda(z - z_0), \tag{1b}$$

where $\epsilon' = 1 - (Re_c/Re)^2$, A is a generalized amplitude coefficient, u_n and w_n are the radial and axial shape factors found by following Davey's analysis, λ is the fundamental axial wavenumber, and z_0 is a term to shift the vortices axially in the annulus. The first two terms of equation (1) were fit to the entire set of experimental results shown in figure 1 by varying A, λ, and z_0 in a least-squares sense to achieve the best match. Using these values of A, λ, and z_0 in the first two terms of equation (1) provided the curves in figure 2. The match between the Davey solution and the experimental data is quite good at the lower Reynolds number ($Re = 103$), given the spatial resolution of the experiments. Although both measurements of the Fourier components of the velocity field (Gollub & Freilich 1976; Berland *et al.* 1986; Heinrichs *et al.* 1988) and direct measurement of the azimuthal velocity (Wereley & Lueptow 1994) have previously confirmed the validity of the Davey solution, these results show that the radial and axial velocity also fit the Davey solution. The experiments match the Davey solution less well at the higher Reynolds number ($Re = 124$). Particularly noticeable are the higher experimental values for the radial velocity in outflow regions at axial positions of $\zeta = 0.7$ and 2.7. This is not surprising given that the Davey expansion is most appropriate very near the transition to Taylor vortex flow ($\epsilon' = 0$) and has been shown to deviate from experimental results as ϵ' becomes greater than 0 (Wereley & Lueptow 1994). Furthermore, by including only the first two terms of the expansion, the higher wavenumber modes are excluded, making it difficult for the solution to be as peaked as the experimental data. The fact that the measurements show sharper gradients than the Davey solution indicates that spatial averaging, which is unavoidable in correlation-based PIV, is not a problem for the results presented in this paper.

The increasing strength of the vortices relative to the velocity of the inner cylinder with increasing Reynolds number is evident in the velocity profiles of figure 2. Increasing the Reynolds number from just above transition to supercritical flow ($Re = 103$) to just below the transition to wavy vortex flow ($Re = 124$) results in more than doubling the maximum radial and axial velocities. Even so, the maximum radial and axial velocities corresponding to the secondary flow are only about 2–7% of the velocity of the inner cylinder, a velocity scale of the primary flow.

The asymmetry in inflow (negative v_r) and outflow (positive v_r) regions is evident in the radial velocity profile, shown in figure 2(*a*). At the higher Reynolds number, the maximum outflow velocity is nearly twice the maximum inflow velocity, consistent with Snyder & Lambert's description of higher radial velocities at outflow regions (Snyder & Lambert 1966). The difference in the outflow and inflow velocities affects the widths of the two regions. The width of the inflow region is 1.3 times that of the outflow region, as measured between zero-crossings. The differences between the inflow and outflow radial velocities are less distinct near the transition Reynolds number, but still noticeable. The inflow and outflow velocities should be symmetric as ϵ' approaches zero.

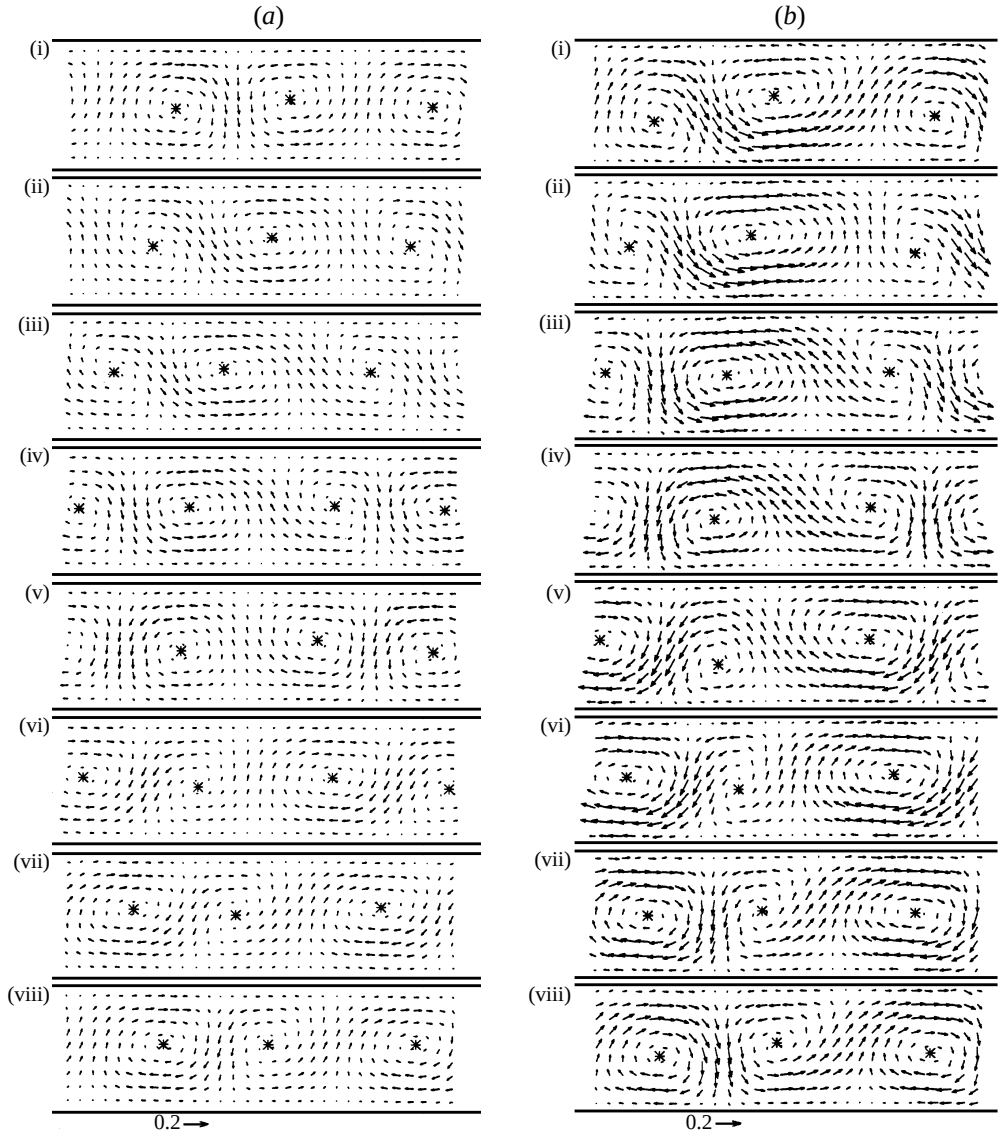

FIGURE 3(*a*, *b*). For caption see facing page.

Apart from the expected sign change, the axial velocity is asymmetric with respect to the centre of the annular gap, as shown in figure 2(*b*). The maximum positive axial velocity in the inner part of the gap is larger in magnitude than the minimum negative velocity in the outer part of the gap, regardless of Reynolds number. This is a result of mass conservation given the difference in flow area for the positive inner axial flow and the outer negative axial flow.

3.2. *Wavy vortex flow*

The traditional flow visualization of wavy vortex flow by observing the motion of small particles or dye at a clear outer cylinder suggests that the vortices passing a point on the outer cylinder oscillate axially. Although there is evidence that the structure is more complex (Bust, Dornblasser & Kochschmieder 1985) the simplest idea is that of a stack

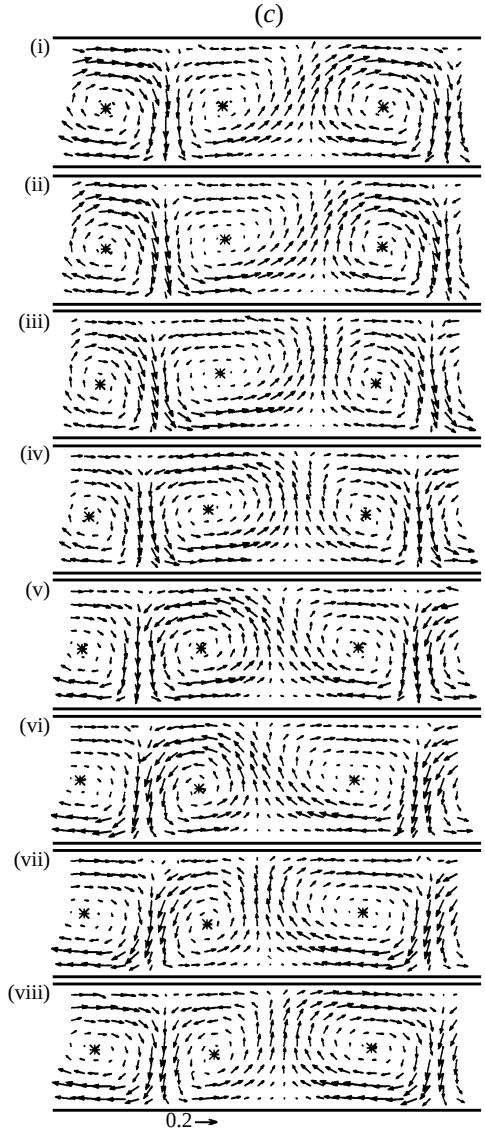

FIGURE 3. Velocity vectors in a radial plane for wavy vortex flow. (*a*) Just above transition to wavy vortex flow, $Re = 131$, $\epsilon = 0.28$ (two azimuthal waves); (*b*) $Re = 253$, $\epsilon = 1.48$ (four azimuthal waves); (*c*) $Re = 927$, $\epsilon = 8.09$ (four azimuthal waves). The arrow at the bottom of each figure corresponds to $0.2\, r_i \Omega$. The rotating inner cylinder is the upper boundary and the fixed outer cylinder is the lower boundary of each frame.

of closed cell vortices that undulate in the axial direction with identical phase. This, however, is not the appearance of the flow at a Reynolds number of $Re = 131$, just above the transition to wave vortex flow, shown in figure 3. In figure 3, the annulus is horizontal, and time progresses from top to bottom through one complete cycle of an azimuthal wave passing the measurement plane. The ensemble-averaged vector fields at eight evenly spaced times during an azimuthal wave are shown in figure 3. The vector fields were ensemble averaged over 2 to 18 waves depending on the Reynolds number and sampling frequency.

Although the axial motion of the vortices is evident based on the location of the vortex centres, marked by asterisks, the significant transfer of fluid between adjacent vortices indicates that vortex cells are not independent. The transfer of fluid occurs in a cyclic fashion with a particular vortex gaining fluid from adjacent vortices and then losing fluid to adjacent vortices. Similar results occur at significantly higher Reynolds numbers of $Re = 253$ and $Re = 927$, shown in figures 3(*b*) and 3(*c*). It is evident from the velocity vectors that the degree of transfer of fluid is greater at $Re = 253$ than at either the higher or lower Reynolds numbers. This notion is addressed in a quantitative fashion below.

The cycle can be described most easily with reference to the middle vortex in figure 3(*b*) for $Re = 253$. The cycle begins with fluid from the inner part of the left-hand vortex flowing into the middle vortex and toward the outer cylinder. Simultaneously, fluid from the middle vortex moves into the right-hand vortex and toward the inner cylinder. The result is that fluid winds around the outer side of the middle vortex from left to right. The flow out of the right-hand side of the middle vortex ends in frame (ii) of figure 3(*b*), so that now the middle vortex is gaining fluid from the left-hand vortex without losing any fluid. By frame (iii) of figure 3(*b*), an inward flow from the right-hand vortex also feeds fluid into the middle vortex. The flow into the middle vortex decreases in the fourth frame as the flow in from the left-hand vortex ends. In frames (iv)–(vii) the process reverses, beginning with flow around the inner side of the middle vortex from right to left, followed by flow out of the middle vortex to the left, then flow out to the left and right, and finally to the right only. Of course the middle vortex is losing the same amount of fluid during the second half of the cycle as it gained in the first half. The second half of the cycle (frames (v)–(viii)) appears identical to the first half of the cycle (frames (i)–(iv)) reflected either about an outflow boundary between the left-hand and middle vortices or about an inflow boundary between the middle and right-hand vortices. This is called 'shift-and-reflect' symmetry (Marcus 1984). A consequence of the shift-and-reflect symmetry is that the flow associated with one vortex is identical to the flow associated with an adjacent vortex half a cycle later, reflected about a radial line. The degree to which the shift-and-reflect symmetry is accurate is addressed later in this paper.

As a consequence of the shift-and-reflect symmetry, adjacent vortices possess a character that can loosely be described as 'out of phase' with each other. For instance, when the middle vortex is gaining fluid in frame (iii) of figure 3(*b*), the adjacent right-hand vortex is losing fluid, and the converse in frame (vii). When flow is around the outside of the middle vortex in frame (i), the flow is around the inside of the adjacent right-hand vortex, and the converse in frame (v).

The implication of this cyclic transfer of fluid between adjacent vortices is a cyclic structure in the entire flow field. Referring again to figure 3(*b*), fluid generally winds around the vortices twice during the cycle. In frames (iv) and (v) there is a winding flow from right to left, and in frames (viii) and (i) there is a winding flow from left to right. A similar winding flow occurs for rotating Couette flow with an axial flow superimposed on it when the axial flow is relatively strong (Lueptow 1995; Büchel *et al*. 1996; Stöckert & Lueptow 1998). In between the winding flow sequences, every second vortex shrinks as fluid flows out of it (middle vortex in frames (vi) and (vii) while adjacent vortices gain that same fluid and grow. The global cycle can be described as winding flow, growth-shrinkage of vortices, winding flow, and shrinkage-growth of vortices.

The effect of the Reynolds number on the flow is evident from comparing figures 3(*a*), 3(*b*) and 3(*c*). Clearly, the vortices become stronger with increasing Reynolds

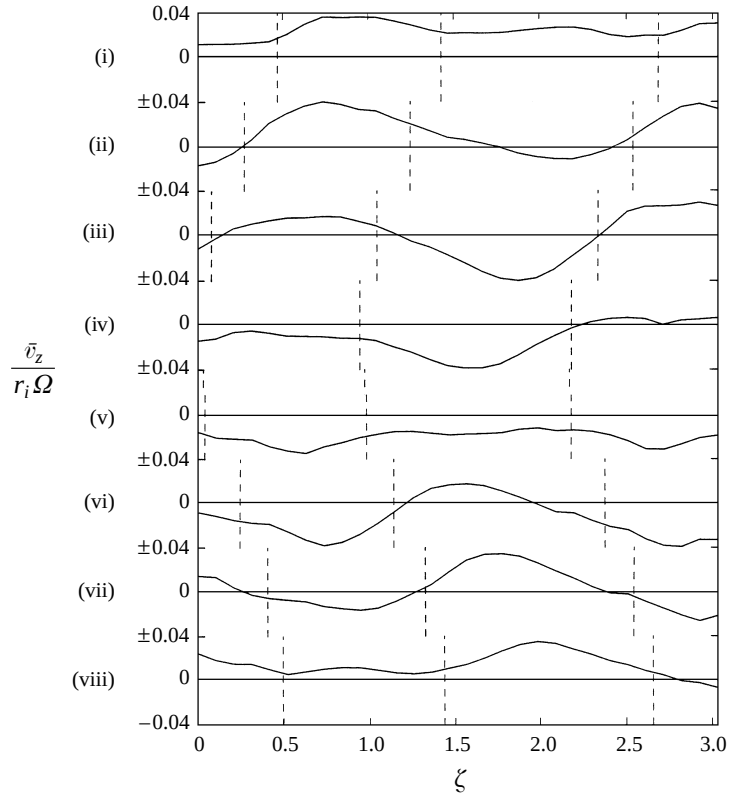

FIGURE 4. Average axial velocity as a function of axial position for $Re = 253$ ($\epsilon = 1.48$) at the eight time instants corresponding to those shown in figure 3(*b*). Axial locations of vortex centres are marked by vertical dashed lines. Positive values correspond to flow to the right in figure 3(*b*).

number, consistent with LDV measurements of the azimuthal velocity (Wereley & Lueptow 1994). The axial motion of the vortex centres is evident in figures 3(*a*) and 3(*b*), but the vortex centre motion is diminished at the higher Reynolds number in figure 3(*c*). Likewise, the transfer of fluid between vortices is evident at the lower Reynolds numbers, particularly $Re = 253$ in figure 3(*b*). However, at the higher Reynolds number in figure 3(*c*), the axial flow is reduced, particularly at the outflow boundaries. This results in less apparent winding flow at the higher Reynolds number. Several of these differences in the flow field and the dependence of these differences on the Reynolds number are addressed in more detail below.

The net axial flow is quantified in figure 4 for $Re = 253$. To generate this figure, the instantaneous axial flow rate at each axial position at which vectors appear was found by numerically integrating the axial component of velocity. From this, $\bar{v}_z$, the radially averaged axial velocity at that axial location, was determined. The 8 plots in figure 4 correspond to the 8 frames in figure 3(*b*). The axial positions of the vortex centres are marked with vertical dashed lines. When fluid winds around the vortices to the right, as in frames (i) and (viii) of figure 3(*b*), the axial flow rate is generally positive. Conversely, when flow winds around the vortices to the left, as in frames (iv) and (v) of figure 3(*b*), the axial flow is generally negative. In frames (ii) and (iii) of figure 4, the positive axial flow on the left-hand side of the middle vortex and the negative axial flow on the right-hand side of the middle vortex combine to feed fluid to the middle vortex.

The converse occurs in frames (vi) and (vii) when there is a net loss of fluid from the middle vortex. Similar results occur at all of the other Reynolds numbers considered, including the lowest Reynolds number for wavy vortex flow, $Re = 131$.

In the case of supercritical circular Couette flow with an imposed axial flow, the vortices translate axially in the annulus with a velocity somewhat larger than the average axial velocity (DiPrima & Pridor 1979; Ng & Turner 1982; Lueptow, Docter & Min 1992). Similarly, one would expect that the vortices in wavy vortex flow would translate axially to the right when the axial flow is positive at all axial positions, and vice versa. From figure 4, it is evident that the maximum axial flow occurs concurrent with the vortex centre reaching its axial extrema. For instance in frames (iv) and (v) of figure 4, the axial flow is generally leftward (negative), and the vortex centre position is at its leftmost position at the same instant. Likewise, rightward, shown in frames (i) and (viii), corresponds to the vortex being at its rightmost position. The axial translation of the vortex generally occurs when there is essentially no net axial flow, such as the leftward vortex motion in frames (ii) and (iii) of figure 4.

It is helpful to express the instantaneous average axial velocity in terms of an instantaneous axial Reynolds number, $Re_a = \bar{v}_z d/\nu$. This Reynolds number characterizes the instantaneous magnitude of the local axial flow winding around the vortices. The maximum of this instantaneous axial Reynolds number that was achieved during the azimuthal wave cycle is shown in figure 5(*a*) as a function of the reduced Reynolds number, $\epsilon = Re/Re_c - 1$, for both positive and negative axial flow. The difference between the values for positive and negative flow indicate the degree of error in the experiments and data analysis. To put the magnitude of the instantaneous axial Reynolds number in context, it is useful to compare it to the effect of similar axial Reynolds numbers on the stability of circular Couette flow with an axial through-flow. For instance, at rotating Reynolds numbers just above the transition to supercritical flow ($\epsilon = 0^+$), an axial Reynolds number of 9–20 results in helical rather than toroidal vortices (Snyder 1962; Schwarz, Springett & Donnelly 1964; Chung & Astill 1977; Takeuchi & Jankowski 1981; Lueptow *et al.* 1992). For $1 \leqslant \epsilon \leqslant 5.5$, axial Reynolds numbers of the magnitude of those in this study would result in wavy vortices that change shape rapidly with frequent dislocations (Lueptow *et al.* 1992). Thus, while the instantaneous axial Reynolds numbers are not exceptionally large, they are not insignificant when compared to results for supercritical circular Couette flow with an axial flow.

Another way of expressing the degree of axial flow is to consider the volume fraction of a vortex that is transferred into and out of a vortex during one azimuthal wave period. To do this, it is necessary to first define the volume of a vortex. The instantaneous boundary of a vortex, defined as the axial location at which extrema in the radially averaged radial velocity occur, correspond to radial inflow and outflow regions. The distance between either two outflow or two inflow regions corresponds to the instantaneous wavelength of the vortex. The average wavelength was found by averaging the instantaneous wavelength over one azimuthal wave. The average vortex volume is then easily found from the average wavelength and the geometry of the apparatus. The volume of fluid transferred axially across the instantaneous boundary was found by integrating the axial velocity across the annular gap at the axial position of the instantaneous boundary of a vortex. Figure 5(*b*) shows the fraction of the total volume of a vortex that is transferred axially into and out of the vortex during one azimuthal wave, based on the absolute value of the volume of fluid transferred axially (both right and left) normalized by the average vortex volume. Of course, the net volume of fluid transferred axially over an entire azimuthal wave must be zero to

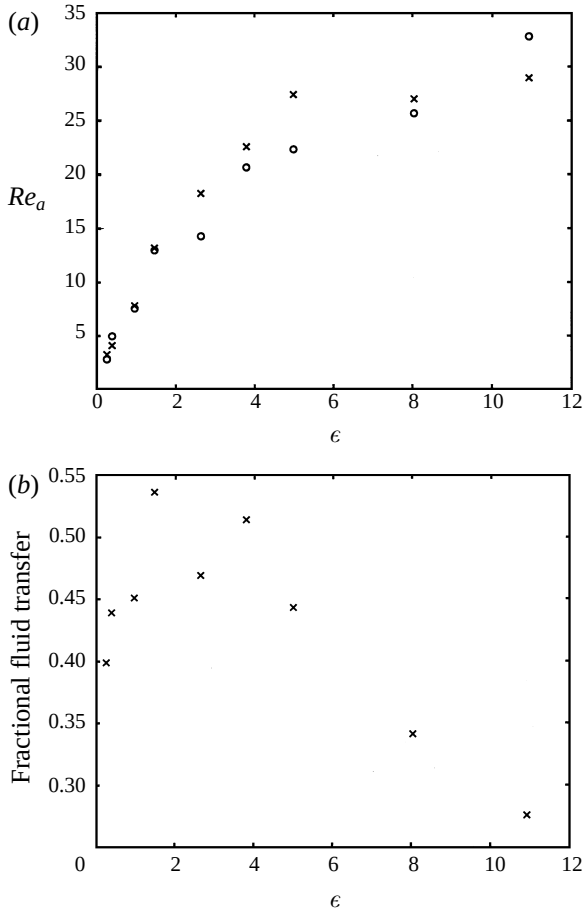

FIGURE 5. (*a*) Dependence of maximum instantaneous axial Reynolds number on the reduced Reynolds number. ×, positive axial flow; ○, negative axial flow. (*b*) Fraction of the average volume of a vortex that is pumped into and out of the vortex in one wave period.

maintain mass conservation, so the volume of fluid transferred either into or out of a vortex is half that indicated in figure 5(*b*).

The volume of fluid pumped into and out of a wavy vortex is substantial. In some cases, the fraction of the volume of a vortex that is transferred is over one-half. This corresponds to one-fourth of the fluid exiting the vortex and then re-entering the vortex within one azimuthal wave. The volume of fluid transferred across the boundaries between vortices reaches a maximum at moderate reduced Reynolds numbers of 1 to 5. At lower Reynolds numbers the volume of fluid transferred into and out of the vortex decreases, probably as a result of the decreased strength of the vortices evident in figure 3. At higher Reynolds number, the fluid transfer also decreases, perhaps corresponding to a decrease in the amplitude of the azimuthal waves discussed below.

Although the data was acquired at a single radial-axial plane for equally spaced timesteps, the travelling-wave character of wavy vortex flow permits the conversion of time domain data into azimuthal angular position θ using the relation $\theta = ct/(r_i + \frac{1}{2}d)$, where c is the azimuthal travelling wave speed and $(r_i + \frac{1}{2}d)$ is the radius at the centre of the annular gap. The travelling wave speed was calculated using the fundamental frequency found from the ensemble average of the spectra of the time histories of the

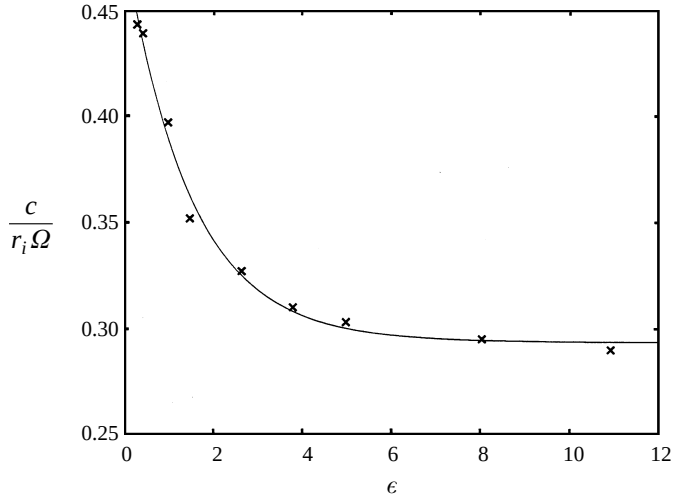

FIGURE 6. Azimuthal wave speed normalized by the surface speed of the inner cylinder, $c/\Omega r_i$. Curve is a least-squares fit to exponential decay.

axial and radial velocity at all points measured in the flow. The results, shown in figure 6, indicate that the wave speed normalized by the surface speed of the inner cylinder, $c/\Omega r_i$, decreases monotonically as the reduced Reynolds number is increased approaching an asymptotic value of 0.294 times the surface velocity of the inner cylinder, consistent with other results for wavy vortex flow (Coles 1965; Jones 1981; King *et al.* 1984; Marcus 1984; Schroder & Keller 1990).

The spatial distribution of the axial flow based on converting time domain data into azimuthal position is presented in figure 7 for three Reynolds numbers. In this figure, the axis of rotation is vertical and the azimuthal position along the centre of the annulus is normalized by the gap width, $\gamma = (r_i + \frac{1}{2}d)\,\theta/d$. Consider first figure 7(*b*) for $Re = 253$. For this particular Reynolds number four waves appeared around the annulus so the azimuthal length of one wave at the centre of the annular gap is $8.45d$. The vertical boundaries of the figure are periodic. The horizontal boundaries of the figure correspond to the axial extent of the PIV measurement domain. In this figure, dotted contours correspond to upward axial flow, dashed contours correspond to downward axial flow, and solid contours correspond to zero axial flow. In addition, the axial positions of the vortex centres and boundaries between vortices are indicated by the heavy solid curves. Since flow visualization of wavy vortex flows is usually done with small reflective flakes that align with the flow to result in dark bands at inflow and outflow regions (Kataoka 1986), the curves marking the boundaries between vortices correspond approximately to the bands in flow visualization (Burkhalter & Koschmieder 1973; Andereck *et al.* 1986).

Perhaps the most striking feature of figure 7(*b*) is the axially elongated regions, or vertical strips, of axial flow, both upward and downward, along the axial length of the test cell. For instance, at an azimuthal position of $3.5 \leqslant \gamma \leqslant 4.8$ the axial flow is downward, whereas for $0 \leqslant \gamma \leqslant 0.5$ and $7.5 \leqslant \gamma \leqslant 8.5$ the flow is upward. These vertical strips of axial flow correspond to instances in figure 3 where the fluid is winding around a vortex. The direction of the axial flow corresponds to the direction in which the vortex tube is distorted. In other words, downward axial flow corresponds to a valley in the azimuthal wave, and upward flow corresponds to a peak in the wave. This result is consistent with the results for rotating Couette flow with an imposed axial

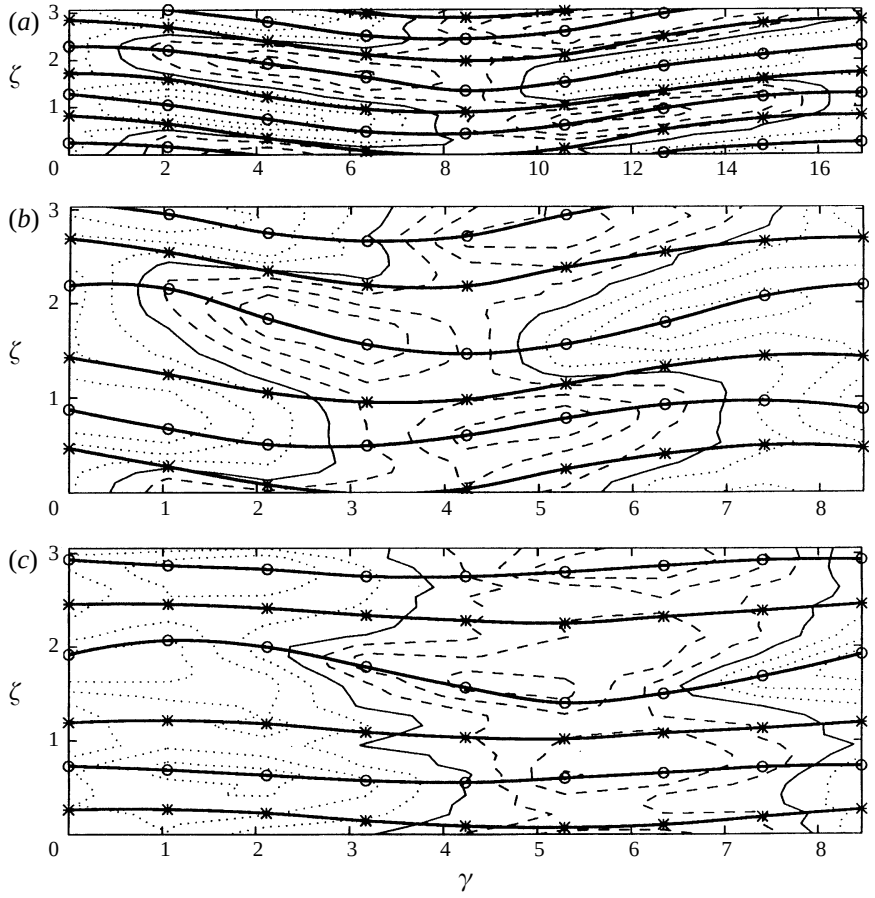

FIGURE 7. Contour plot of the spatial distribution of axial flow at the centre of the annular gap. Solid contours are zero axial flow; dotted contours are positive axial flow; dashed contours are negative axial flow. Contours are evenly spaced so that four contours appear between zero and the maximum or minimum values. Solid curves marked with asterisks correspond to the axial position of the vortex centres. Solid curves marked with circles correspond to the axial position of the boundaries between vortices. (*a*) $Re = 131$, $\epsilon = 0.28$; (*b*) $Re = 253$, $\epsilon = 1.48$; (*c*) $Re = 927$, $\epsilon = 8.09$.

flow, where the vortices translate in the direction of the axial flow (DiPrima & Pridor 1979; Ng & Turner 1982; Lueptow *et al.* 1992).

The curves corresponding to centres of the vortices tend to follow the horizontal sections of the zero axial flow contours. On the other hand, the curves corresponding to vortex boundaries map along the positive and negative maxima for the axial flow. These maxima in the axial flow at one vortex boundary occur at the same time that there is nearly zero net axial flow at the vortex centre and across the boundary on the opposite side of the vortex. For instance, there is a maximum in the downward flow through the boundary at an azimuthal position of $\gamma = 2.7$ and an axial position of $\zeta = z/d = 1.67$. Yet there is almost no axial flow at the vortex centre at an axial position of $\zeta = 1.0$ and at the boundary at an axial position of $\zeta = 0.5$, both just below this maximum downward flow. This corresponds to the situation of the right-hand vortex feeding fluid into the middle vortex shown in figure 3. Situations where fluid enters both the top and the bottom of the vortex correspond to regions in figure 7(*b*) where positive contours at a lower vortex boundary and negative contours at an upper vortex

boundary overlap in the azimuthal direction, such as occurs for the middle vortex in figure 7(*b*) at $\gamma = 1.8$. The opposite situation, where fluid simultaneously exits both the top and the bottom of the vortex, correspond to negative contours at the lower boundary and positive contours at the upper boundary, such as at $\gamma = 6.0$ for the middle vortex in figure 7(*b*).

The effect of Reynolds number on the axial flow is evident considering figures 7(*a*) and 7(*c*); for $Re = 131$ and $Re = 927$, respectively, in comparison with figure 7(*b*). Note that at $Re = 131$ only two azimuthal waves appear around the circumference of the test cell, so the azimuthal wave extends to $\gamma = 16.9$. It is evident that at this lower Reynolds number the azimuthal overlap of regions of upward and downward axial flow has greater azimuthal extent, about $6d$, than at $Re = 253$ where the overlap is only about $2d$ wide. At the same time, the vertical strips of pure positive or negative axial flow are nearly the same width (about $2d$). On the other hand, at the higher Reynolds number shown in figure 7(*c*), the azimuthal overlap of regions of upward and downward axial flow extend only a short distance azimuthally (less than $2d$). The vertical strips of pure axial flow are about $3d$ wide, somewhat wider than at the lower Reynolds numbers. Similar figures of the flow for other Reynolds numbers are consistent with these results.

A typical appearance of flow visualization of wavy vortex flow at high Reynolds numbers is a boundary that has large-amplitude waviness with boundaries above and below that have a much smaller amplitude of waviness (Coles 1965; Kataoka 1986; Donnelly 1991). This same character is evident in figure 7(*c*). The middle boundary, which is an inflow boundary, has a large waviness. In contrast, the adjacent upper and lower outflow boundaries in the figure have substantially smaller amplitude waviness. To our knowledge, the cause of this phenomenon has not been discussed elsewhere, although Marcus (1984) showed a similar result for numerical simulation of wavy vortex flow. Some insight into this result is gained by referring back to figure 3(*c*) for the same Reynolds number as shown in figure 7(*c*), where it is clear that the radial outflow regions are much stronger than the inflow regions. In addition, there is much less axial flow at outflow regions than at inflow regions. This suggests that the waviness of the boundary is directly related to the degree of fluid transfer between vortices. Because of the strong radial flow in outflow regions the axial flow that transfers fluid between vortices is suppressed leading to reduced waviness at outflow boundaries between vortices. On the other hand, the weaker radial flow at inflow regions permits an axial transfer of fluid between the vortices on either side of the inflow region resulting in a more wavy inflow boundary.

In addition to the periodic character of the flow into and out of adjacent vortices, the vortex centres move both axially and radially in a cyclic fashion. Figure 8 shows the trajectory of two adjacent vortex centres bounding a radial inflow region through the passage of one azimuthal wave, corresponding to one complete cycle around the curves. The vortex associated with the path on the left rotates CCW, and the vortex associated with the path on the right rotates CW. The distance between the dotted horizontal lines corresponds to the middle half of the annular gap $[(r_i + \frac{1}{4}d) \leqslant r \leqslant (r_i + \frac{3}{4}d)]$, and the top of the figure is toward the inner cylinder. The sense of the motion of the vortex centre along the trajectory is shown by the arrows in the figure. The axial trajectories of a pair of vortex centres are in phase. In other words, the vortex centres reach their farthest right positions and farthest left positions at the same time. Upon leftward motion of a vortex pair, the CCW vortex moves radially outward, whereas the CW vortex moves radially inward, and vice versa for motion to the right. Thus, the radial motion of the vortex centres is out of phase.

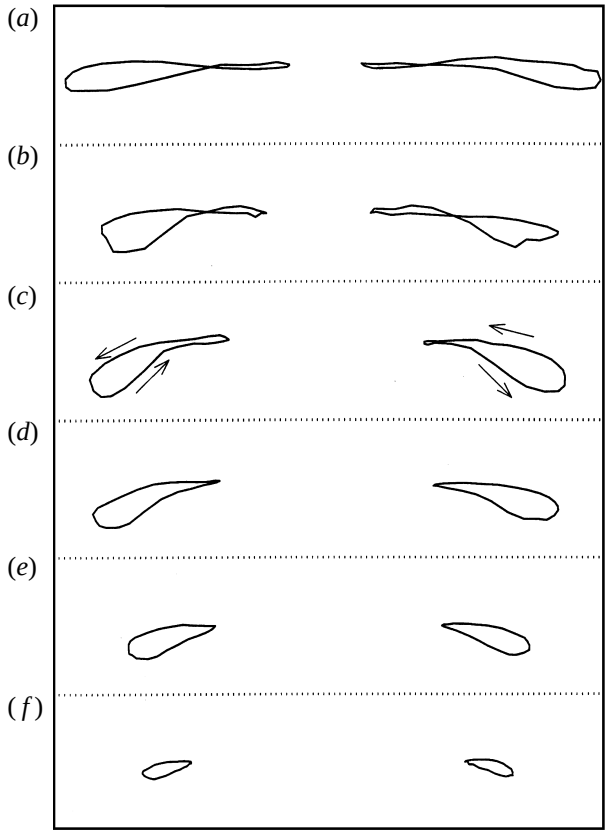

FIGURE 8. Mapping of the vortex centre path for an adjacent pair of vortices (CCW on the left-hand side and CW on the right-hand side) with an inflow region between them. Arrows indicate the direction that the vortex centre proceeds along the paths. From top to bottom $Re = 131$, 202, 253, 373, 615, 1221; $\epsilon \approx 0.28$, 0.98, 1.48, 2.66, 5.03, 10.97.

The radial motion of the vortex centres increases to a maximum at $Re = 253$ and then decreases with increasing Reynolds number. Of course, the axial and radial motion at the lower and upper limits, corresponding to non-wavy Taylor vortex flow and non-wavy turbulent vortex flow, is zero, so the tendency for the motion to decrease as these limits are approached is not surprising. Perhaps more interesting is the aspect ratio of axial to radial motion of the vortex centres. At low Reynolds numbers the axial motion is substantially greater than the radial motion. As the Reynolds number increases, the aspect ratio decreases, although the axial motion is always greater than the radial motion. At lower Reynolds numbers, the path of the vortex centre is a figure of eight nearly aligned to the walls. At higher Reynolds numbers, the path of the vortex centres becomes paisley-shaped with the major axis of the adjacent vortex centre paths at alternating slight angles to the walls. In the latter cases, the centre of one vortex moves towards the wall, while the centre of the adjacent vortex moves away from the wall. The instant at which the vortex centre is closest to a wall corresponds to the instant that fluid is winding around the opposite side of the vortex, as is evident in figure 3(*b*). In fact, the radial translation of the vortex centre is related to the degree of axial flow. For instance, in figure 5(*b*) the maximum axial flow occurs for $Re = 253$ ($\epsilon = 1.48$), which clearly has the greatest axial translation shown in figure 8. Likewise low axial flow rates at high and low Reynolds numbers correspond to minimal radial

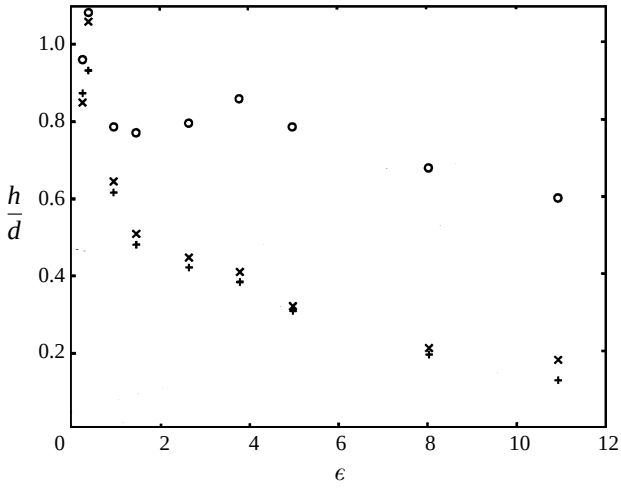

FIGURE 9. Azimuthal wave height normalized by the gap width measured at ×, vortex centres; ○, inflow boundaries; and +, outflow boundaries.

motion of the vortex centres. Thus, the axial winding flow around the vortices acts to shift the vortices toward the wall opposite the axial flow. Similar results have been obtained computationally for Taylor vortex flow with an imposed axial and radial flow (Lueptow & Hajiloo 1995).

The axial motion of the vortex centres is one measure of the amplitude of the azimuthal waviness. However, the amplitude of the waves, h, can also be measured in terms of the motion of the inflow boundaries and outflow boundaries between vectors. All three measures are plotted in figure 9 as a function of the reduced Reynolds number. At low reduced Reynolds numbers all three measures indicate a wave amplitude of about one gap width. For $\epsilon > 1$, however, the amplitude of the motion of centres and outflow boundaries are nearly equal and decrease to a small fraction of the gap width with increasing Reynolds number. On the other hand, the axial motion of inflow boundaries remains a significant portion of the gap width. The net effect is the character evident in figure 7(*c*), where the boundaries associated with inflow are quite wavy, while the boundaries associated with outflow are nearly flat. Bust *et al.* (1985) measured the wave height axial distance between crest and troughs of waves observed at the surface of the outer cylinder. They found that, for $\epsilon > 1$, the wave height was as much as $1.2d$ for water and about half this value for 10 cSt silicone oil. In our case, where the viscosity is 3.1 cSt, between that of water and silicone oil, the wave height measured at the inflow boundaries is between that of water and silicone oil measured by Bust *et al.*, although the wave height at the outflow boundaries and centres is substantially less. Bust *et al.* could not explain the curious dependence of the wave amplitude on the viscosity of the fluid, although they suggested that it might be related to their observation of the vortex height at the wall of the outer cylinder or end effects. The measurements in figure 9, however, are not based on the appearance of the vortex at the wall of the outer cylinder, nor are they for such a small aspect ratio as used by Bust *et al.* They also found that for $0 < \epsilon < 1$, the wave height increases from zero to a maximum at $\epsilon = 1$, in contrast to the results in figure 9 that show a maximum in wave height for $0 < \epsilon < 1$. The difference may be attributable to the experimental methods and locations at which the wave height was measured.

We finally address the 'shift-and-reflect' symmetry that has been used in

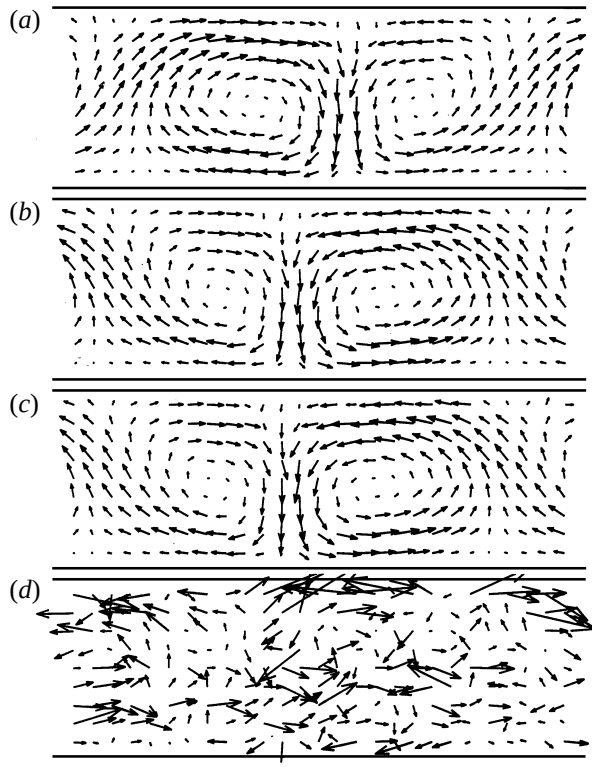

FIGURE 10. (*a*) Velocity vector field for a time instant at $Re = 615$. (*b*) Reflected velocity vector field corresponding to the velocity vector field in (*a*) after shifting axially to minimize the error with (*c*). (*c*) Velocity vector field half a cycle after that shown in (*a*). (*d*) Vector difference between velocity vectors in (*b*) and (*c*) magnified by a factor of 10.

computational models of wavy vortex flow as a strategy to minimize computations (King *et al*. 1984; Marcus 1984). The shift-and-reflect symmetry refers to the apparent similarity of the velocity field, observed at a particular azimuthal position and time, to the velocity field observed at the same azimuthal position half a period later reflected axially about a vortex boundary. Although Marcus justified the use of shift-and-reflect symmetry by noting the decay of Fourier modes that do not obey the shift-and-reflect symmetry, the time-resolved velocity fields shown in figure 3, can be used to validate experimentally the assumption of shift-and-reflect symmetry. To accomplish this, the velocity field at one time instant was compared to the velocity field at a time instant half a cycle later, as illustrated in figure 10. The original velocity field, figure 10(*a*) was reflected about the centre of the figure to produce figure 10(*b*). In general, it was necessary to shift the reflected velocity field axially to minimize the error between the reflected velocity field and the velocity field half a cycle later, figure 10(*c*). The error between the velocities at any given axial position of the reflected flow field was the absolute value of the difference between the speeds of the actual velocity and the reflected velocity, normalized by the average of the two speeds. The overall error between the two velocity fields was based on the spatial average of the error at all vector positions in the velocity field averaged over all time instants in one azimuthal wave cycle. Based on this approach, the axial shift of the reflected velocity field was chosen as the position for which the overall error between the actual velocity field and the reflected velocity field was smallest.

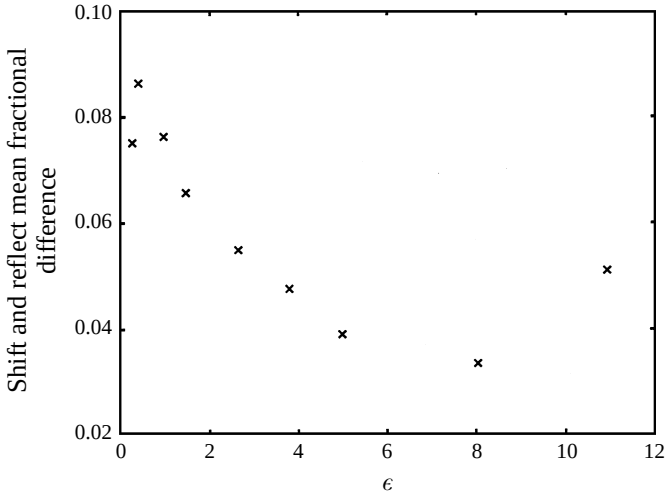

FIGURE 11. Fractional difference between the reflected velocity field and the velocity field half a cycle later.

The reflected velocity field in figure 10(*b*) is nearly identical to the velocity vector field half a cycle later, shown in figure 10(*c*). The vector difference between the two velocity fields is shown in figure 10(*d*), with the difference velocity field amplified by a factor of 10 compared to the velocity fields in figure 10(*a*)–10(*c*). The space and time averaged normalized error for the Reynolds numbers studied is quite small, as shown in figure 11. The error in using the shift-and-reflect symmetry assumption is greatest at the lowest Reynolds numbers, but the shift-and-reflect symmetry assumption is clearly quite reasonable over the entire range of Reynolds numbers considered.

4. Conclusions

Above the transition from subcritical circular Couette flow to non-wavy Taylor vortices, the velocity field in the annulus is much as one might expect based on flow visualization. The vortices are independent cells, the vortical motion of which grows as the rotating Reynolds number increases. Even so, the axial and radial velocities are more than an order of magnitude less than the maximum azimuthal velocity. The velocity field matches the Davey perturbation expansion well at Reynolds numbers near transition, but deviates somewhat from the theory as the Reynolds number increases. The deviation is probably due both to the limited number of terms included in the expansion and the fact that the Davey analysis is most accurate near the transition Reynolds number.

At Reynolds numbers above the second supercritical transition, that to wavy vortex flow, the velocity field is much more complex. In fact, the motion of the vortices and the degree of fluid exchange between vortices is quite different from what one would expect based on flow visualization experiments. The vortices themselves move axially, but there is also substantial radial motion of the vortex centres. The radial motion of adjacent vortices is out of phase so that when one vortex moves radially inward, the adjacent vortices move radially outward. The axial motion decreases continually as the Reynolds number increases, but the radial motion has a maximum at a moderate Reynolds number above that for transition. The radial motion of the vortex toward

either wall is accompanied by a generally axial flow winding around the opposite side of the vortex, not unlike the winding flow around vortices when an axial through-flow is superimposed upon circular Couette flow. The result is that there are regions of net axial flow in the direction of the axial deformation of the vortex tube at particular azimuthal locations along the azimuthal wave. Azimuthally adjacent to these regions are regions where an individual vortex grows in size while the two adjacent vortices become smaller, and vice versa. This action transfers a substantial portion of the fluid from one vortex to an adjacent vortex and back throughout one azimuthal wave. Since wavy vortex flow consists of a stack of wavy vortices that are in phase, the fluid motion at any particular location along the length of an azimuthal wave extends axially. Thus, there is an axially elongated region, or strip, of net axial flow of one sense, a vertical strip where alternating vortices are losing fluid, a vertical strip of axial flow of the opposite sense, and a vertical strip where the vortices that were losing fluid are now gaining fluid. These alternating strips of axial flow and fluid transfer propagate around the annulus of the circular Couette flow device at the azimuthal wave speed. Finally, the concept of shift-and-reflect symmetry appears to be valid for wavy vortex flow.

This work was supported by the National Science Foundation.

REFERENCES

Andereck, C. D., Liu, S. S. & Swinney, H. L. 1986 Flow regimes in a circular Couette system with independently rotating cylinders. *J. Fluid Mech.* **164**, 155–183.

Berland, T., Jøssang, T. & Feder, J. 1986 An experimental study of the connection between the hydrodynamic and phase-transition descriptions of the Couette–Taylor instability. *Phys. Scripta* **34**, 427–431.

Brandstater, A. & Swinney, H. L. 1987 Strange attractors in weakly turbulent Couette–Taylor flow. *Phys. Rev.* A **35**, 2207–2220.

Büchel, P., Lücke, M., Roth, D. & Schmitz, R. 1996 Pattern selection in the absolutely unstable regime as a nonlinear eigenvalue problem: Taylor vortices in axial flow. *Phys. Rev.* A **53**, 4764–4777.

Burkhalter, J. E. & Koschmieder, E. L. 1973 Steady supercritical Taylor vortex flow. *J. Fluid Mech.* **58**, 547–560.

Bust, G. S., Dornblaser, B. C. & Koschmieder, E. L. 1985 Amplitudes and wavelengths of wavy Taylor vortices. *Phys. Fluids* **28**, 1243–1247.

Chung, K. C. & Astill, K. N. 1977 Hydrodynamic instability of viscous flow between rotating coaxial cylinders with fully developed axial flow. *J. Fluid Mech.* **81**, 641–655.

Coles, D. 1965 Transition in circular Couette flow. *J. Fluid Mech.* **21**, 385–425.

Davey, A. 1962 The growth of Taylor vortices in flow between rotating cylinders. *J. Fluid Mech.* **14**, 336–368.

DiPrima, R. C. & Pridor, A. 1979 The stability of viscous flow between rotating concentric cylinders with an axial flow. *Proc. R. Soc. Lond.* A **366**, 555–573.

DiPrima, R. C. & Swinney, H. L. 1985 Instabilities and transition in flow between concentric rotating cylinders. In *Topics in Applied Physics*, *Hydrodynamic Instabilities and the Transition to Turbulence* (ed. H. L. Swinney & J. P. Gollub), pp. 139–180. Springer.

Donnelly, R. J. 1991 Taylor–Couette flow: The early days. *Physics Today* **44**, November 32–39.

Dring, R. P. 1982 Sizing criteria for laser anemometry particles. *Trans. ASME* I: *J. Fluids Engng* **104**, 15–17.

Fasel, H. & Booz, O. 1984 Numerical investigation of supercritical Taylor-vortex flow for a wide gap. *J. Fluid Mech.* **138**, 21–52.

Gollub, J. P. & Freilich, M. H. 1976 Optical heterodyne test of perturbation expansions for the Taylor instability. *Phys. Fluids* **19**, 618–626.

Gollub, J. P. & Swinney, H. L. 1975 Onset of turbulence in a rotating fluid. *Phys. Rev. Lett.* **35**, 927–930.

Heinrichs, R. M., Cannell, D. S., Ahlers, G. & Jefferson, M. 1988 Experimental test of the perturbation expansion for the Taylor instability at various wavenumbers. *Phys. Fluids* **31**, 250–255.

Jones, C. A. 1981 Nonlinear Taylor vortices and their stability. *J. Fluid Mech.* **102**, 249–261.

Jones, C. A. 1985 The transition to wavy Taylor vortices. *J. Fluid Mech.* **157**, 135–162.

Kataoka, K. 1986 Taylor vortices and instabilities in circular Couette flows. In *Encyclopedia of Fluid Mechanics* (ed. N. P. Cheremisinoff), pp. 237–273. Gulf Publishing Company.

King, G. P., Li, Y., Lee, W., Swinney, H. L. & Marcus, P. S. 1984 Wave speeds in wavy Taylor-vortex flow. *J. Fluid Mech.* **141**, 365–390.

Kose, K. 1994 Spatial mapping of velocity power spectra in Taylor–Couette flow using ultrafast NMR imaging. *Phys. Rev. Lett.* **72**, 1467–1470.

Lueptow, R. M. 1995 *Fluid mechanics of a rotating filter separator*. Advances in Filtration and Separation Technology, Nashville, TN, American Filtration and Separations Society.

Lueptow, R. M., Docter, A. & Min, K. 1992 Stability of axial flow in an annulus with a rotating inner cylinder. *Phys. Fluids* A **4**, 2446–2455.

Lueptow, R. M. & Hajiloo, L. 1995 Flow in a rotating membrane plasma separator. *Am. Soc. Artif. Int. Organs J.* **41**, 182–188.

Majumdar, A. K. & Spalding, D. B. 1977 Numerical computation of Taylor vortices. *J. Fluid Mech.* **81**, 295–304.

Marcus, P. S. 1984 Simulation of Taylor–Couette flow. Part 2. Numerical results for wavy-vortex flow with one travelling wave. *J. Fluid Mech.* **146**, 65–113.

Meyer, K. A. 1967 Time-dependent numerical study of Taylor vortex flow. *Phys. Fluids* **10**, 1874–1879.

Meyer, K. A. 1969 Three-dimensional study of flow between concentric rotating cylinders. *High-Speed Computing in Fluid Dynamics: Phys. Fluids Suppl. II*, **12**, II-165–II-170.

Meyer-Spasche, R. & Keller, H. B. 1980 Computations of the axisymmetric flow between rotating cylinders. *J. Comput. Phys.* **35**, 100–109.

Moser, R. D., Moin, P. & Leonard, A. 1983 A spectral numerical method for the Navier–Stokes equations with applications to Taylor–Couette flow. *J. Comp. Phys.* **52**, 524–544.

Ng, B. S. & Turner, E. R. 1982 On the linear stability of spiral flow between rotating cylinders. *Proc. R. Soc. Lond.* A **382**, 83–102.

Schroder, W. & Keller, H. B. 1990 Wavy Taylor-vortex flows via multigrid-continuation methods. *J. Comput. Phys.* **91**, 197–227.

Schwarz, K. W., Springett, B. E. & Donnelly, R. J. 1964 Modes of instability in spiral flow between rotating cylinders. *J. Fluid Mech.* **20**, 281–289.

Snyder, H. A. 1962 Experiments on the stability of spiral flow at low axial Reynolds numbers. *Proc. R. Soc. Lond.* A **265**, 198–214.

Snyder, H. A. & Lambert, R. B. 1966 Harmonic generation in Taylor vortices between rotating cylinders. *J. Fluid Mech.* **26**, 545–562.

Stöckert, M. & Lueptow, R. M. 1998 Velocity field for Taylor Couette flow with an axial flow. *Phys Fluids* (submitted).

Takeda, Y., Fischer, W. E. & Sakakibara, J. 1994 Decomposition of the modulated waves in a rotating Couette system. *Science* **263**, 502–505.

Takeuchi, D. I. & Jankowski, D. F. 1981 A numerical and experimental investigation of the stability of spiral Poiseuille flow. *J. Fluid Mech.* **102**, 101–126.

Taylor, G. I. 1923 Stability of a viscous liquid contained between two rotating cylinders. *Phil. Trans. R. Soc.* A **223**, 289–343.

Tsameret, A. & Steinberg, V. 1994 Absolute and convective instabilities and noise-sustained structures in the Couette–Taylor system with an axial flow. *Phys. Rev.* E **49**, 1291–1308.

Wereley, S. T. & Lueptow, R. M. 1994 Azimuthal velocity in supercritical circular Couette flow. *Exps Fluids* **18**, 1–9.

Willert, C. E. & Gharib, M. 1991 Digital particle image velocimetry. *Exps. Fluids* **10**, 181–193.